New Journal of Physics
The open-access journal for physics

Surfactant-driven self-organized surface patterns by ion beam erosion

Kun Zhang, Marc Brötzmann and Hans Hofsäss[1]
II Physikalisches Institut, Universität Göttingen, Friedrich-Hund-Platz 1, 37077 Göttingen, Germany
E-mail: hans.hofsaess@phys.uni-goettingen.de

New Journal of Physics **13** (2011) 013033 (20pp)
Received 22 September 2010
Published 24 January 2011
Online at http://www.njp.org/
doi:10.1088/1367-2630/13/1/013033

Abstract. In this paper, we report on the self-organized pattern formation on Si surfaces driven by Fe surfactant atoms. Si substrates were irradiated with 5 keV Xe ions at normal incidence and ion fluences up to 5×10^{17} Xe^{+} cm^{-2} under continuous deposition of Fe surfactant atoms. In the absence of Fe deposition, uniform flat surfaces were obtained. With Fe surfactants, pronounced patterns, such as dots, combinations of dots and ripples and ripples with about 100 nm wavelength, were generated. The Fe coverage and deposition direction determine the pattern type and the pattern orientation, respectively. A critical Fe steady-state coverage for onset of dot formation and onset of ripple formation ranges between 2×10^{15} and 6×10^{15} Fe cm^{-2}. With increasing ion fluence, the pattern contrast increases but the pattern type remains unchanged. The surface region consists of a thin amorphous Fe_xSi layer with $x \approx 0.2$ in the ripple and dot regions and $x \approx 0.03$ in the intermediate regions. Pattern formation is explained by ion-induced diffusion and phase separation of the initially flat amorphous Fe_xSi layer and subsequent ion beam erosion with composition-dependent sputter yield. Directed deposition of Fe causes preferential deposition and shadowing and determines the final pattern orientation and morphology.

[1] Author to whom any correspondence should be addressed.

Contents

1. Introduction 2
2. Experimental 4
3. Results 6
4. Scenario for pattern formation 13
5. Discussion 16
6. Conclusion 18
Acknowledgments 18
References 19

1. Introduction

Ion beam sputtering-induced surface nanopatterns have received considerable theoretical and experimental attention due to the complex physical mechanism of self-organization, which has not been fully understood [1]–[5], and their potential applications in fabricating large-area self-organized nanostructured surfaces on a variety of materials [6]–[10]. Pattern formation induced by noble gas ion beam sputtering has been extensively studied for silicon substrates, silica surfaces and single-crystalline and polycrystalline metal substrates. In particular, silicon substrates are very attractive as a monoatomic model system, because they are easily amorphized with low-fluence ion irradiation. Thus, silicon is an ideal substrate for comparison with continuum theories of ion beam erosion without considering the crystal structure. Modeling self-organized pattern formation is based on continuum theories, such as the linear model of Bradley and Harper [11], extensions to nonlinear terms and noise using the Kuramoto–Sivashinsky equation [3, 12, 13], modifications regarding the ion-related response functions [14] and also Monte Carlo simulations using solid-on-solid models [4]. These models are able to predict the formation of ripple-type nanopatterns for large ion incidence angles, typically $>45^\circ$ with respect to the surface normal. For ions incident under the normal and near-normal directions, the theoretical models predict uniform and flat surfaces in agreement with experimental findings, e.g. for ion beam erosion of Si with inert noble gas ions (the present work and [15, 16]). The theoretical models also correctly predict a rather abrupt change in the ripple orientation from a wave vector parallel to the projected ion beam direction to a wave vector oriented perpendicular on increasing the ion incidence angle over 60°–75°, depending on the ion species and substrate [17].

In our recent work, we have introduced surfactant sputtering as a novel technique for the erosion of surfaces, utilizing the steady-state coverage of the surface with typically 10^{14}–10^{16} atoms cm^{-2} of foreign or self-atoms simultaneously during ion beam sputtering [18]–[21]. This is achieved by controlled slow co-deposition of surfactant atoms during ion beam erosion, so that net erosion is maintained and saturation coverage of the surface with surfactant atoms is rapidly established at ion fluences as low as 10^{16} cm^{-2}. These foreign or self-atoms then act as surface-active agents (surfactants). Depending on the chemical bonding with substrate atoms, the surfactant atoms may form nanosized clusters on the top of the surface, e.g. for Ag on Si [18], or contribute to ultrathin compound film formation due to recoil implantation, ballistic mixing, ion-induced interdiffusion and alloy formation. Examples of the

latter case are ultrathin nanostructured silicide [20] and carbide films [21] formed on Si and amorphous carbon substrates. Surfactant-assisted ion beam erosion allows one to manipulate the sputtering erosion of substrate atoms in manifold ways and on length scales from the nanometer range to macroscopic dimensions. As a consequence, self-organized pattern formation processes during ion beam erosion are drastically modified not only by intentionally deposited surfactant atoms but also by unintentionally deposited contaminants.

Earlier studies of ion beam erosion under simultaneous co-deposition were devoted to cone formation or relief surface structure formation during sputter erosion of metal and silicon substrates [22]–[27] and to the investigation of the sputter yield amplification effect [28]–[32]. The most prominent example of cone formation during ion beam erosion is the unusual behavior of Mo on Si and some metal surfaces, leading to pronounced cone patterns [24], [33]–[39]. However, in these studies, the formation of a steady-state surface coverage was hardly observed. Instead the observed cone formation was described as due to Mo seeding, suggesting an initial seeding mechanism rather than a dynamic equilibrium or a steady-state situation.

In several experimental studies, unusual formation of dot patterns on compound semiconductor surfaces was observed for normal ion incidence on GaSb [40, 41], InSb [42] and InP [43] as well as for near-normal ion incidence of 25°–42° on GaAs and InP [44]. Recently, this pattern formation was explained as self-sustained etch masking [45] due to continuous segregation of one component as a result of preferential sputtering effects. This mechanism is rather similar to surfactant sputtering or processes leading to cone formation; however, the surfactants are not deposited but are continuously enriched at the compound substrate surface due to preferential sputtering.

Reports by Frost *et al* [48], Ziberi *et al* [47], [49–51] and Ling *et al* [52] on the ion beam erosion of Si surfaces with keV noble gas ions have shown the formation of different types of dot, hole and ripple nanopatterns for a wide regime of ion incidence angles, surprisingly also for near-normal ion incidence angles between 0° and 30°. The type of pattern seemed to depend rather sensitively on the ion incidence angle. There have been attempts to extend continuum theories based on the nonlinear Kuramoto–Sivashinsky equation towards an anisotropically generalized non-local equation to model the observed unusual pattern formation, in particular dot pattern formation at normal ion incidence, but with limited success [5, 46]. Recently, Macko *et al* [53] have proved that the observed diversity of patterns is due to Fe contamination of the Si surface introduced during sputter erosion. In their study, a co-deposition of Fe from a stainless steel target irradiated together with the silicon substrate was carried out using 2 keV Kr^+ ions at an ion incidence angle of 30°. The irradiation setup was similar to that used by our group for surfactant sputtering studies [18]. They observed a large variety of nanopatterns ranging from dot to ripple patterns, whereas no patterns were formed without Fe co-deposition (the present work and [15, 16]). Qualitatively, the study clearly shows that the type of pattern generated depends on the amount of co-deposited Fe, i.e. the steady-state Fe coverage. In addition, the study provides evidence that the pattern orientation depends on the deposition direction of the incident Fe atoms, similar to observations in early studies of relief pattern formation by ion bombardment [22]. Sánchez-García *et al* [54] recently demonstrated the formation of nanodot and nanohole patterns on Si induced by 1 keV Ar^+ ion beam erosion at normal ion incidence. Here, the pattern formation was caused by the incorporation of Fe and Mo contaminants with concentrations of up to $3.5 \times 10^{15}\,\mathrm{cm}^{-2}$ originating from sputter erosion of the ion source cathodes as well as substrate holder parts. The experiments carried out by Macko *et al* [53] and Sánchez-García *et al* [54] describe, in essence, a surfactant sputtering process. The previously

mentioned large variety of patterns observed by Frost *et al* [48], Ziberi *et al* [47], [49–51] and Ling *et al* [52] for sputtering of Si at near-normal ion incidence can thus be easily explained by unintentional contamination of the substrate, most likely due to the Fe atoms sputtered off the vacuum chamber wall.

In this paper, we investigate the nanopattern formation on Si surfaces by surfactant sputtering using 5 keV Xe ions at normal incidence and co-deposition of Fe surfactant atoms. A low Fe steady-state coverage is achieved by simultaneous sputtering of the Si substrate and an adjacent inclined steel target, which is simultaneously exposed to the ion beam. Steel was chosen as the sputter target because it resembles the walls of the vacuum chamber, which may be exposed to an ion beam unintentionally. The pattern morphology, wavelength, amplitude and orientation, as well as the sputter yield, are quantitatively analyzed as a function of ion fluence, Fe steady-state coverage and Fe-deposition direction. Furthermore, the microstructure and composition of the patterned surface were analyzed by transmission electron microscopy (TEM), energy dispersive x-ray spectroscopy (EDX) and Rutherford backscattering spectroscopy (RBS), revealing the formation of a thin amorphous Fe_xSi surface layer.

2. Experimental

For the surfactant sputtering studies, we have used single-crystalline Si(100) substrates of size $7 \times 10\,\mathrm{mm}^2$, with measured root mean square (rms) surface roughness < 0.1 nm. The substrates were cleaned sequentially in an ultrasonic bath with acetone and methanol. A 5 keV Xe^+ ion beam with a low beam divergence of about 12 mm diameter was provided by a low-energy mass selected Colutron® ion beam system using a Wien-filter mass selection and a beam sweep system [24]. The ion flux on the substrate was about $1\,\mu\mathrm{A\,cm}^{-2}$. All substrates were kept at room temperature and irradiated under high vacuum conditions of 2×10^{-6} Pa with the ion beam incident along the normal direction of the Si surface.

Previous studies have shown that sputtering of Si surfaces at normal ion incidence without surfactants produces rather flat and uniform surface topography without any indication of pattern formation [15, 16]. To confirm this with our experimental setup and to ensure that our irradiations are free of unintentional contaminations, we have carried out irradiation of Si with 5 keV Xe^+ ions at normal ion incidence and incidence angle of up to 30° for ion fluences of up to $2 \times 10^{18}\,\mathrm{cm}^{-2}$.

For surfactant-assisted erosion studies, the source of Fe surfactant atoms was a steel target (9SMnPb28K free cutting steel, $< 0.14\%$ C, $< 0.11\%$ P, $< 0.33\%$ S, $< 0.01\%$ N, $< 1.3\%$ Mn, 0.05% Si, $< 0.35\%$ Pb) positioned adjacent to the Si substrate at inclination angles of 20°–60° of its surface normal relative to the ion beam direction. One half of the ion beam irradiated the Si substrate, while the other half simultaneously irradiated the steel target. The irradiation setup is schematically shown in figure 1. Sputtered Fe atoms are deposited with a certain incidence angle distribution of 60°–90° with respect to the surface normal and within about ±45° in-plane azimuthal angle. With such a geometrical arrangement, a fraction of atoms sputtered off the surfactant target were directly deposited with a low kinetic energy of a few tens of eV onto the Si substrate. The Fe-deposition flux varies across the Si substrate and allows one to study the erosion effects as a function of surfactant coverage.

The surface morphology of the irradiated Si substrates was analyzed by atomic force microscopy (AFM) in contact mode using a Nanosurf microscope over an area of $3 \times 3\,\mu\mathrm{m}^2$. For the tip, we used AFM probe-type PPP-CONTR Si cantilevers from NanoAndMore GmBH with

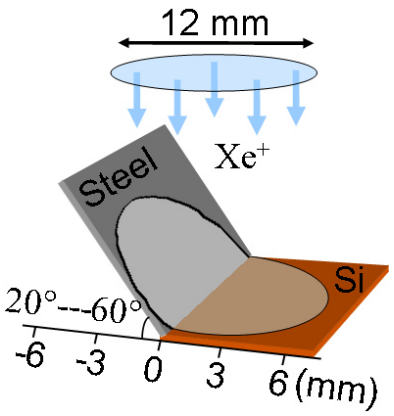

Figure 1. Schematic experimental setup for surfactant sputtering. A Si substrate is irradiated with 5 keV Xe ions at normal ion incidence. A steel sputter target is mounted adjacent to the Si substrate at inclination angles between 20° and 60°, and this is sputtered by the same ion beam. The sputtered Fe atoms are partially deposited onto the Si surface with the lowest deposition flux for the most distant position on the Si substrate.

a mean tip radius of < 7 nm. AFM measurements were carried out using Nanosurf Easyscan software. For topography analysis as well as statistical analysis and Fourier transformation, we used the open source software Gwyddion. Rutherford backscattering spectroscopy (RBS) with 900 keV He^{++} ions and a beam spot of 1 mm diameter was used to quantitatively determine the average Fe coverage on different spots of the Si samples with and without ion beam erosion of the Si substrate. The sputtering yields were measured with mechanical surface profilometry. The microstructure of iron-silicide nanopatterns was analyzed using TEM and EDX using a 200 kV Philips CM 200-UT microscope equipped with a field emission electron source and for imaging a 4 megapixel cooled CCD sensor. The scanning mode of the microscope allows the measurement of EDX line scans along a defined path. TEM sample preparation was performed using a focused ion beam (FIB) system. This preparation technique requires deposition of a Pt cover layer. In order to spatially separate the Si-Fe surface from this Pt layer in the TEM images, the samples were coated with an amorphous carbon capping layer prior to TEM sample preparation. The capping layer was deposited using 100 eV low-energy carbon ion beam deposition [55].

Simulations of sputtering yields, ion and recoil distributions and ballistic mixing were performed using the Monte Carlo codes SRIM 2003–2008 [56] and the TRIDYN [57]. The TRIDYN surface binding energy input parameters were slightly adjusted to reproduce measured sputter yields for Si and Fe erosion with Xe ions, as well as corresponding SRIM sputter yields. It should be noted that SRIM versions 2008 and 2010 give much lower sputter yields for light elements such as Si or C compared to version 2006 and earlier versions, TRIDYN and experimental values. On the other hand, the angular emission distribution of sputtered light atoms such as Si or C atoms is completely different in SRIM version 2006 and earlier versions.

The Fe-deposition flux on the Si substrate is low enough to ensure a net positive erosion rate and rapid establishment of a steady-state surfactant coverage. The saturation coverage establishes already for ion fluences as low as $1 \times 10^{16}\,\mathrm{cm}^{-2}$ [19]. TRIDYN simulations for

our erosion condition show that the saturation coverage is reached after about $3 \times 10^{16}\,\mathrm{cm}^{-2}$. In the present study, we used ion fluences between 1×10^{17} and $5 \times 10^{17}\,\mathrm{ions\,cm}^{-2}$ and thus investigated the pattern formation under steady-state coverage conditions. The relative local deposition flux at different spots on the substrate was calculated assuming a $\cos^{y}\theta$ angular emission distribution of sputtered atoms with $y \approx 1$–1.5 [58, 59] and the given substrate–target geometry. It turns out that the Fe coverage across the substrate varies up to a factor of 5 with the lowest coverage at the most distant point from the sputter target. This is in agreement with the local Fe-deposition flux, measured in irradiation experiments with an aluminum shield in front of the Si substrate. In this situation, surfactant atoms are sputtered off the steel target and deposited on the Si substrate, on which no sputtering takes place.

For a steel co-sputter target inclined at 30° to the beam direction, we measured the deposition ratio of 0.04–0.12 Fe atoms per Xe ion at different positions on the substrate and a resulting steady-state Fe coverage of 2.5–$5.5 \times 10^{15}\,\mathrm{Fe\,cm}^{-2}$. This is larger compared to the saturation value of $1 \times 10^{15}\,\mathrm{Fe\,cm}^{-2}$ obtained from TRIDYN simulations [57] for pure ballistic mixing of Fe and Si by the Xe ion beam. The larger saturation value may be explained by pronounced ion beam-induced diffusion of Fe into subsurface regions.

Besides Fe as the major surfactant component, there is also a low fraction of $< 1\%$ of C, P, S, Mn and Pb, as constituents of the free cutting steel used, which are expected to play a negligible role in our study. The carbon sputter yield from SRIM simulations [56] is lower than 0.05 atom ion^{-1} for 5 keV Xe incident on steel. From RBS analyses of the sputtered Si substrates, we can give an upper limit for a coverage with Pb of $< 5 \times 10^{12}\,\mathrm{cm}^{-2}$, i.e. at least three orders of magnitude lower compared to the Fe coverages. However, the residual concentration of Xe in the irradiated layer is about $10^{15}\,\mathrm{Xe\,cm}^{-2}$ or about 2 at.%. Macko *et al* [53] also considered indirect erosion due to ions reflected or backscattered from the co-deposition sputter target. In our case, the total fraction of Xe ions backscattered from the steel surface is at most 6% according to SRIM simulations. The fraction arriving at the Si substrate is even smaller. Therefore, we can neglect the influence of indirect erosion.

3. Results

AFM topographic images of Si surfaces, solely sputter eroded with 5 keV Xe ions with a fluence of $5 \times 10^{17}\,\mathrm{cm}^{-2}$, are shown in figure 2. The ion incidence angle was varied between 0° and 30°. The surface remains extremely flat without any surface features even after the removal of about 200 nm of material during the sputter process. The images prove that sputter erosion of Si with noble gas ions at normal and near-normal ion incidence up to 30° without surfactants or contaminations on the surface does not generate any surface patterns. We have repeated these experiments for even higher fluences up to $1 \times 10^{18}\,\mathrm{cm}^{-2}$ and lower ion energies of 2 keV, with the same result.

Topographic AFM images of silicon surfaces, which were irradiated with normal incident Xe ions at a fluence of $5 \times 10^{17}\,\mathrm{ions\,cm}^{-2}$ and for different Fe coverage between 1.8×10^{15} and $1.3 \times 10^{16}\,\mathrm{at.\,cm}^{-2}$, are shown in figure 3. The inset shows the corresponding fast Fourier transform (FFT) images. The indicated Fe coverage was determined by RBS measurements. The large variation in Fe coverage was achieved by a series of erosion experiments, each with a different inclination angle of 20°–60° between the steel target normal and the substrate normal. In figure 3, the projected deposition direction of Fe atoms is from left to right. A clearly discernible dependence of the surface topography on the Fe steady-state coverage is observed.

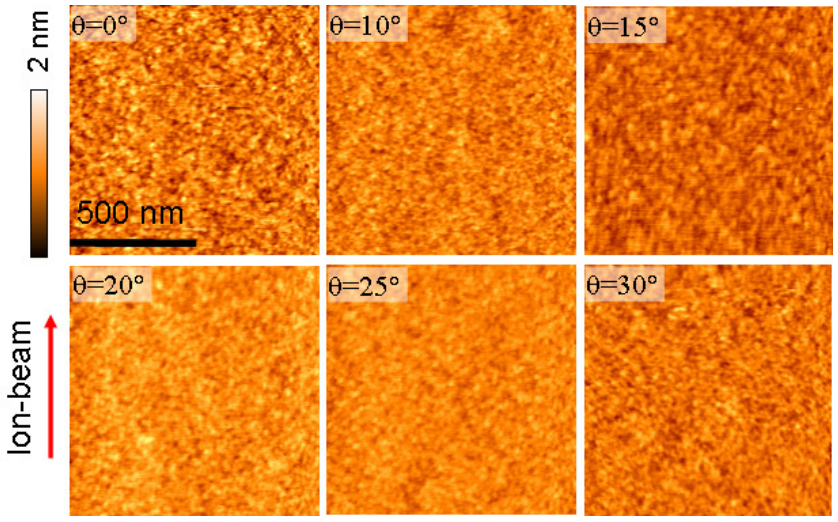

Figure 2. $1 \times 1\ \mu m^2$ topographic AFM images of Si surfaces sputter eroded with 5 keV Xe ions and a fluence of $5 \times 10^{17}\ Xe^+\ cm^{-2}$ with ion incidence angles varying between 0° and 30° with respect to the surface normal. In all cases, the surfaces remain flat with rms roughness below 0.15 nm and no patterns are generated. The arrow indicates the projected ion beam direction for non-zero incidence angles.

No patterns were formed for Fe coverage smaller than 2×10^{15} at. cm^{-2} (figure 3(i)) and the surface remains flat with rms roughness below 1 nm. At an Fe coverage of 2.5×10^{15} at. cm^{-2} (figure 3(h)), a dot pattern appears with dot height varying from 2 to 10 nm. The average dot diameter is 55 ± 8 nm and the dot area density is 135 dots μm^{-2}. The FFT images in figures 3(f)–(h) show an almost isotropic distribution of dots. The power spectral density analysis gives an average dot spacing of about 110 ± 10 nm. For Fe coverage of 3.0 and 3.2×10^{15} at. cm^{-2}, we find a reduced dot area density of 95 and 88 dots μm^{-2}, respectively. The dot diameter and the dot height increase, reaching a diameter of 70 ± 7 and 80 ± 7 nm, and a height of 10 ± 2 and 12 ± 2 nm, respectively. The average spacing increases to about 130 ± 15 nm. As an example, the size distribution of dots extracted with Gwyddion analysis software for the sample shown in figure 3(f) is displayed in figure 4. The majority of dots have a diameter of 80 nm with a Gaussian distribution with full-width at half-maximum (FWHM) = 14 nm (i.e. 80 ± 7 nm). There are also larger dots with diameters up to 150 nm, represented by a Gaussian distribution with a mean diameter of 105 nm and FWHM = 40 nm. Few dots have diameters smaller than 50 nm. At an Fe coverage of 4.0×10^{15} at. cm^{-2} (figure 3(e)), more and more dots are arranged along rows with some dots combining to form short ripples. The average spacing between short ripples or rows of dots is about 120 ± 10 nm. The orientation of the ripples and rows of dots is roughly perpendicular to the projected deposition direction of the Fe atoms. At an Fe coverage of 5.4×10^{15} at. cm^{-2} (figure 3(d)), many short and clearly separated ripple fragments are formed with a length of about a few hundreds of nm. The ripples exhibit a slight curvature and the ripple orientation is slightly non-uniform but almost perpendicular to the projected deposition direction of the Fe atoms (from left to right). Dots appear at dislocations or at points where ripples are interrupted. The wavelength is 110 ± 6 nm. For even higher Fe coverage of $\geqslant 6 \times 10^{15}$ at. cm^{-2} (figures 3(c)–(a)), the dots disappear and a distorted ripple

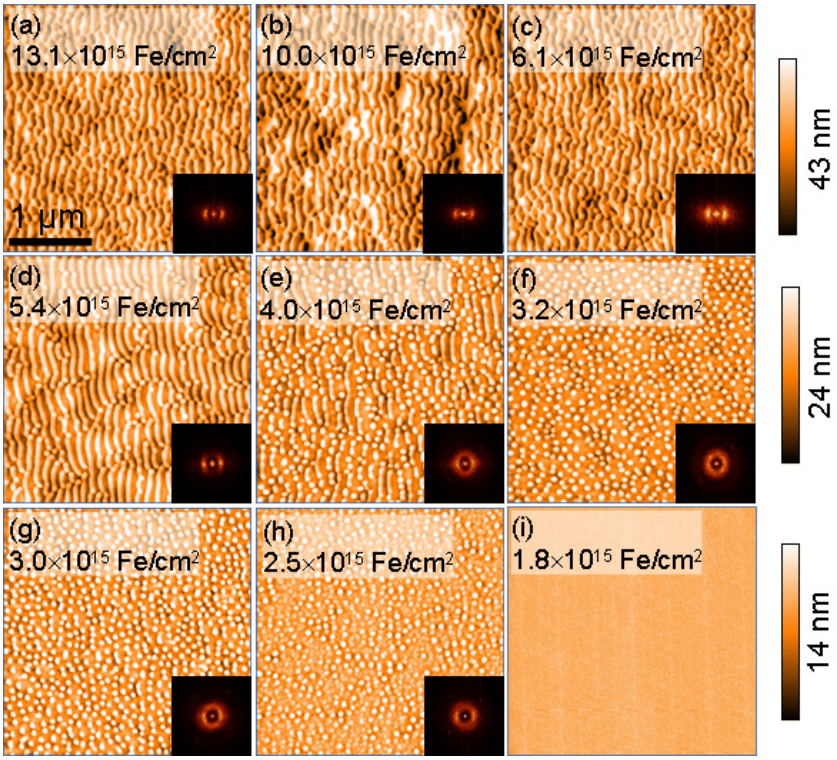

Figure 3. $3 \times 3\,\mu m^2$ topographic AFM images of silicon surfaces irradiated with normal incident Xe ions at a fluence of 5×10^{17} ions cm^{-2} and different Fe steady-state coverages of up to 1.3×10^{16} at. cm^{-2}. A steel target was positioned adjacent to the Si substrate on the left side of the substrate, as shown schematically in figure 1. The projected Fe-deposition direction is from left to right. The corresponding FFT images are shown in the insets. Ripple patterns are generated for Fe coverage exceeding 4×10^{15} at. cm^{-2}.

pattern with many dislocation defects is formed with a ripple wave vector oriented parallel to the projected Fe-deposition direction. The ripple wavelength is 115–125 nm. In these cases, the Fe steady-state coverage is equivalent to 0.7–1.5 nm Fe.

To investigate the role of ion fluence on the nanopattern formation at different Fe coverage, normal incident Xe-ion sputtering has been carried out on Si substrates with ion fluences varied from 1×10^{17} to 5×10^{17} ions cm^{-2}. Adjacent to the Si substrate, a steel surfactant target was mounted with its normal tilted at 30° relative to the ion beam. Figure 5 shows typical AFM images of the Si surface after ion beam erosion with a Fe steady-state coverage of 5.0×10^{15} at. cm^{-2} (figures 5(a)–(c)) and 3.0×10^{15} at. cm^{-2} (figures 5(d)–(f)), respectively. In figure 5, the projected Fe-deposition direction is from left to right. For the Fe steady-state coverage of 5.0×10^{15} at. cm^{-2}, weak nanopatterns of short ripples were observed in addition to dots already appearing for an ion fluence as low as 1×10^{17} ions cm^{-2} (figure 5(a)). The crests of the short ripples are oriented perpendicular to the Fe-deposition direction. The ripples increase in length and height with increasing ion fluence and arrange themselves more and more regularly (figures 5(b) and (c)). At a lower Fe coverage of 3.0×10^{15} at. cm^{-2}, the surface remains flat with an rms roughness of 0.5 nm for ion fluences up to 1×10^{17} ions cm^{-2}. A dot

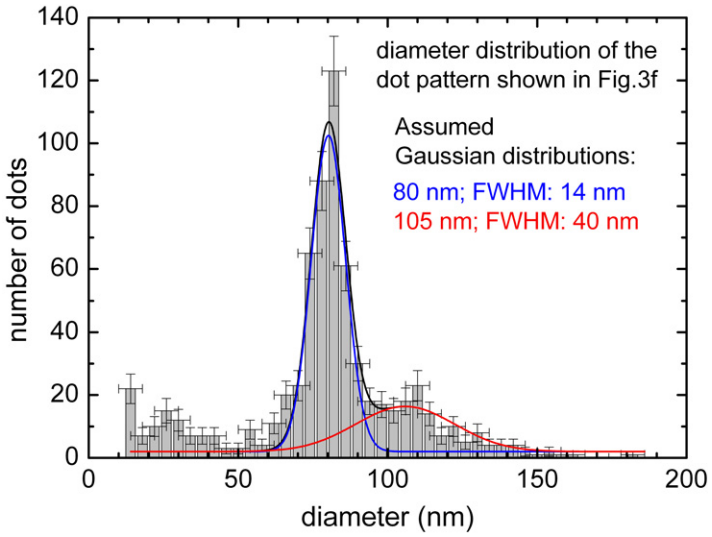

Figure 4. Diameter distribution of dots for the patterns shown in figure 3(f). The error bars indicate the statistical error and the estimated errors of the extracted diameter values. The majority of dots have a mean diameter of 80 nm. The distribution can be described by a Gaussian distribution of FWHM = 14 nm. There are some dots with a diameter smaller than 50 nm and some dots with a diameter up to 150 nm. The distribution of larger dots may be described by a broad Gaussian distribution with a mean diameter of 105 nm and FWHM = 40 nm.

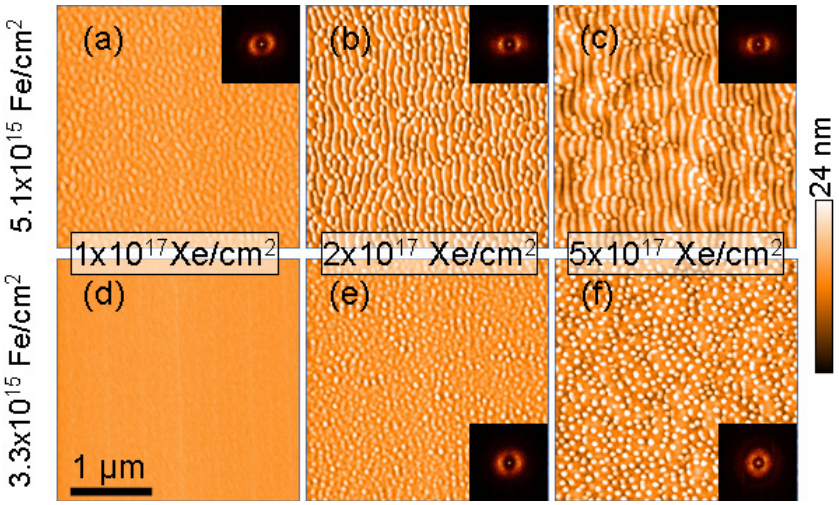

Figure 5. $3 \times 3\ \mu m^2$ topographic AFM images of samples irradiated with 5 keV Xe ions and Fe co-deposition with Fe steady-state coverage of 5×10^{15} at. cm^{-2} (a–c) and 3×10^{15} at. cm^{-2} (d–f) for Xe ion fluence increasing from 1×10^{17} to 5×10^{17} ions cm^{-2}. The projected Fe-deposition direction is from left to right. The corresponding FFT images are shown in the insets.

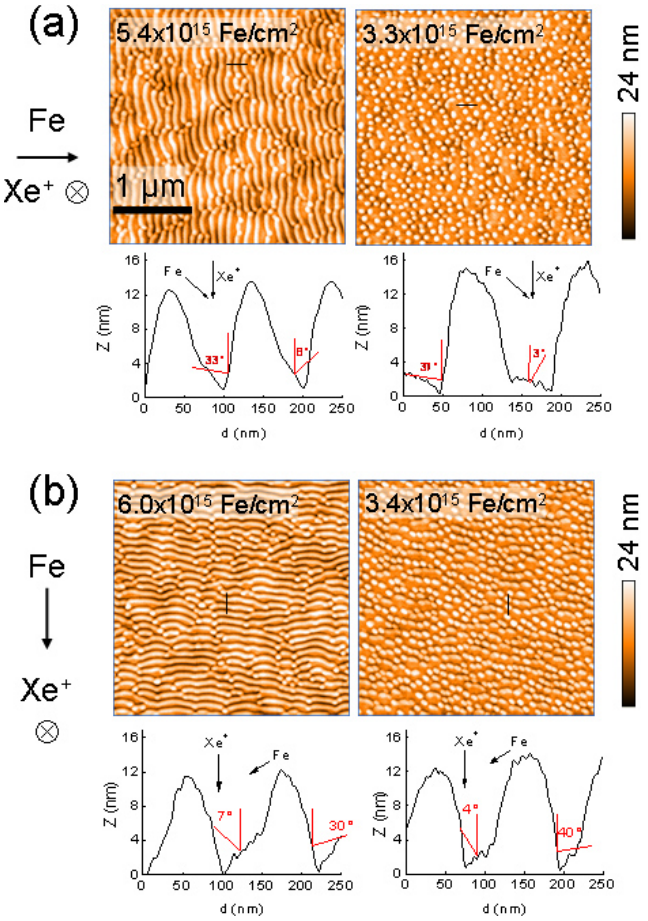

Figure 6. AFM images of ripple and dot patterns created by ion beam erosion of Si substrates with 5 keV Xe ions at normal incidence and Fe co-deposition, resulting in a steady-state Fe coverage of 3.3×10^{15} and 5.4×10^{15} Fe cm^{-2}. The projected direction of Fe co-deposition is from left to right (6a) and from top to bottom (6b). Cross-sectional height profiles from the regions marked by thin black lines are shown below the AFM images. Note that due to different z and d scales, the profiles appear stretched in the z-direction.

pattern starts to form at 2×10^{17} ions cm^{-2} and the dot diameter and dot height increase with further increase in ion fluence. The FFT images indicate an initial weak texture of the pattern, which disappears for dot patterns with increasing dot height. The dot area density decreases from about 150 dots μm^{-2} to about 90 dots μm^{-2} within a certain range of Fe coverage as well as ion fluence. This decrease in density is accompanied by an increase in dot height.

The influence of the Fe-deposition direction on the orientation of the formed nanopatterns becomes obvious by comparing the results from two experiments with different Fe-deposition directions, as shown in figure 6. In one experiment (figure 6(a)), the steel target was positioned on the left side of the Si substrate (i.e. the Fe-deposition direction is from the left), whereas in another setup (figure 6(b)) the steel target was mounted on the top side of the Si substrate (i.e. the Fe-deposition direction is from the top). In both cases Si substrates were irradiated with a normal incident Xe beam and adjacent steel targets with their surface normal tilted towards

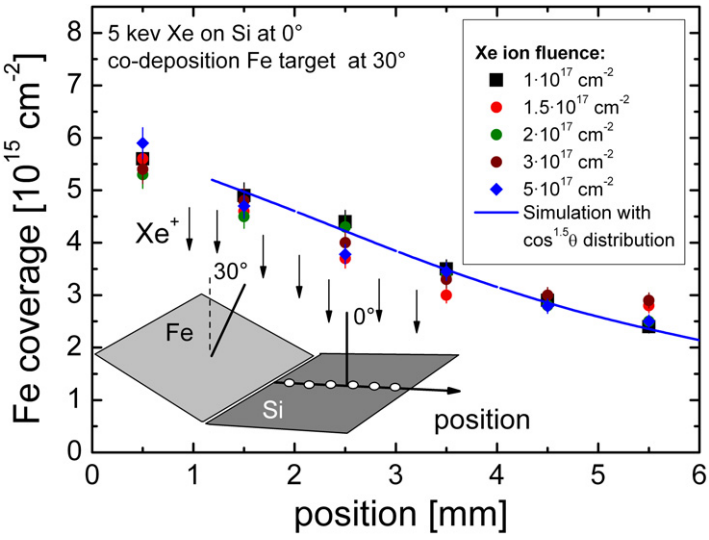

Figure 7. Fe coverage on Si measured with RBS at different positions marked as white dots on the sample for the target–substrate geometry shown and normal incident 5 keV ions for ion fluences between 1×10^{17} and 5×10^{17} cm^{-2}. The solid line is the calculated relative deposition flux assuming a $\cos^{y}\theta$ angular emission distribution of sputtered atoms (see text).

the Si substrate at an angle of 30° with respect to the ion beam. The AFM images in figure 6 clearly show that the orientations of the ripple patterns, mixed patterns of short ripples plus dots and the rows of dots in dot patterns are essentially perpendicular to the Fe-deposition direction, proving that the deposition direction of the surfactant atoms determines the pattern orientation. Representative cross sections of the ripple and dot patterns are also shown in figure 6. The shape of the dots is rather symmetric but the shape of the ripples is asymmetric with the steeper slopes facing the Fe-deposition direction. Also, the regions in between ripples and dots have a weak slope that is also related to the Fe-deposition direction.

In the steady-state condition, the Fe coverage, i.e. the areal density of the deposited Fe surfactant atoms, is independent of the Xe ion fluence and only depends on the ratio between Fe-deposition flux and Xe-ion flux [18]. The Fe coverage was measured with RBS for a deposition ratio up to 0.12 Fe atom per Xe ion and ion fluences between 1×10^{17} and 5×10^{17} ions cm^{-2}. The experimental results shown in figure 7 confirm that for a Xe fluence of 1×10^{17} ions cm^{-2} the Fe coverage has already reached its saturation value. The results are also in good agreement with calculations of the relative deposition flux assuming a $\cos\theta$ angular distribution of sputtered particles, as described in the experimental section.

The patterns formed at different Fe coverages and ion fluences show a characteristic evolution of structure height, structure density and rms roughness. Furthermore, a characteristic evolution of the overall sputter yield is observed. The analysis of the rms roughness and the sputter yield as a function of Fe coverage is shown in figure 8. The evolution of the rms roughness clearly shows a rather well-defined critical Fe coverage for the onset of dot formation (2×10^{15} cm^{-2}), the onset of merging of dots to form ripples (4×10^{15} cm^{-2}) and the onset of ripple formation (6×10^{15} cm^{-2}). In the regime where dot patterns are formed, the dot height increases roughly linear with increasing coverage. In the regimes with mixed dots and short

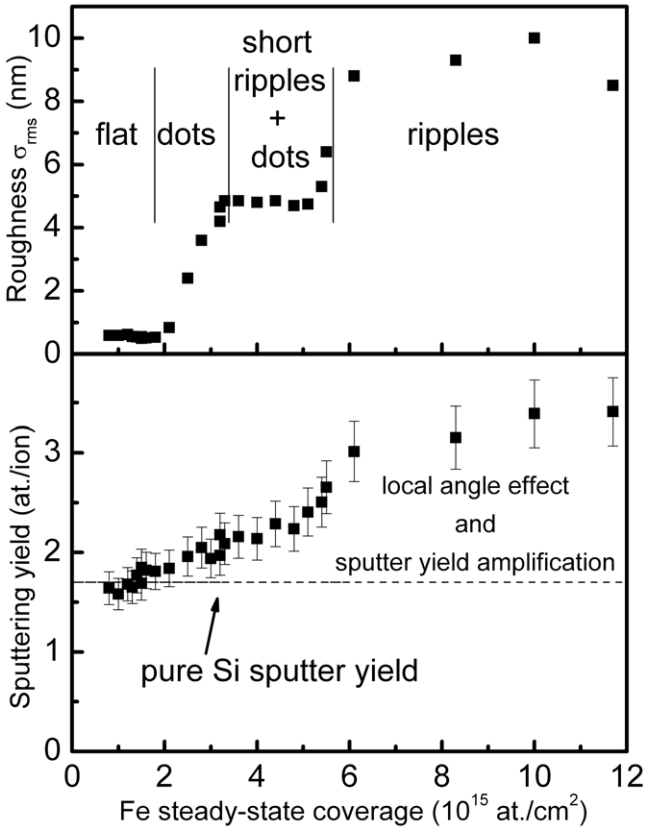

Figure 8. Measured rms roughness (upper graph) and measured sputter yield (lower graph) as a function of Fe steady-state coverage after irradiation with 5 keV Xe at an ion fluence of 5×10^{17} cm^{-2}. The regimes where a flat surface, dots, ripples and mixed dot and ripple patterns occur are indicated.

ripples and also ripples, the rms roughness has almost a constant value. The pattern contrast significantly increases with ion fluence (figure 5).

The measured sputter yield for low Fe coverage corresponds to the sputter yield $Y_{Si} \approx 1.7$ for pure Si. With the onset of dot and ripple formation, the sputter yield increases up to about $Y \approx 3.4$. The reasons for this increase may be (i) the sputter yield amplification effect described by Nender *et al* [30] and Berg *et al* [32] or (ii) an increase in the sputter yield due to the patterned surface leading to local oblique ion incidence. The sputter yield calculated from TRIDYN simulations, which only account for ballistic mixing, is slightly lower than Y_{Si}. Thus ballistic mixing would only be compatible with the sputter yield up to 2×10^{15} Fe cm^{-2} coverage, i.e. within the flat surface regime. The sputter yield amplification effect could only explain the measured maximum sputter yield of $Y \approx 3.4$ for an extreme surface morphology, e.g. consisting of a 1.5 nm buried pure Fe layer and a 0.5 nm top Si layer. However, such a surface morphology is not observed. Based on the measured Fe coverage and depth distribution obtained from RBS, TEM and EDX data, a sputter yield amplification of at most 25% is reasonable. Therefore, the major contribution to the high sputter yield is caused by a local oblique ion incidence due to the patterned surface. In particular, the steeper slopes at the ripple and dot structures are subjected to enhanced sputtering. In the height profiles of the patterns shown in figure 6, the local incidence

angle varies between 0° and 50° and, calculated with SRIM, the local sputter yield may reach values of up to $Y \approx 6$. The average calculated sputter yield is about $\langle Y \rangle \approx 2$–$2.2$. The calculated average sputter yield for height profiles taken from figures 3(a)–(c) gives $\langle Y \rangle \approx 3.2$. Both values are in good agreement with the measured values of the sputter yield displayed in figure 8.

The microstructure and shape of the patterned Fe_xSi layer samples obtained after irradiation with normal incident Xe ions were investigated with TEM and EDX. The initial stage of pattern formation is shown in the TEM image in figure 9(a), obtained after irradiation with 1.5×10^{17} ions cm^{-2} and a Fe steady-state coverage of 3.5×10^{15} cm^{-2}. The amorphous Fe_xSi layer has a thickness of about 15 nm. A weak surface pattern with up to 5 nm amplitude is about to develop. The darker regions in this layer may be due to a non-uniform Fe distribution or film stress. The darker regions in the Si substrate close to the $Si(100)/Fe_xSi$ interface are caused by stress. The cross-sectional TEM images of a sample irradiated with 5×10^{17} ions cm^{-2} and the Fe steady-state coverage of 5.4×10^{15} cm^{-2}, corresponding to the AFM image shown in figure 3(d), are shown in figures 9(b)–(d) with increasing magnification. Prior to the preparation of the TEM samples, a few tens of nm thick amorphous carbon (a-C) film as capping layer was deposited onto the patterned surfaces to ensure good visibility of the Fe_xSi surface. This is necessary because FIB preparation of the TEM samples requires the deposition of a platinum layer, which would have obscured the Fe_xSi surface. With this a-C capping layer the Fe_xSi surface is clearly separated from the topmost Pt layer.

The ripple structure consists of a thin amorphous top layer and appears as a darker region in figures 9(b)–(d). The bright regions are within the crystalline Si substrate and are caused by strain effects. There exists a rather sharp interface to the underlying crystalline Si as can be seen in figure 9(d). The thickness of the amorphous layer in the flat intermediate regions of the ripples is about 15 nm. SRIM simulations reveal a damage profile for 5 keV Xe on Si at normal ion incidence extending up to 15 nm, so that amorphization of the Si substrate up to that depth is expected. TRIDYN simulations of ballistic mixing show a rapidly decreasing Fe concentration with increasing depth extending up to about 15 nm. Therefore, the amorphous Fe_xSi surface layer can thus be explained by ion beam amorphization and forms a dynamic equilibrium situation. The EDX line scans shown in figure 9(e) for the flat region and in figure 9(f) for the ripple region along the black lines marked in figure 9(b) confirm the Fe_xSi composition of the amorphous layer. The EDX line scans reveal an average Fe area density in the ripple region, which is about 6.5 times larger than that of the flat region. For an Fe coverage of 5.4×10^{15} cm^{-2} determined by RBS, we estimate the average composition of the amorphous Fe_xSi as $x \approx 0.03(1)$ for the flat regions and $x \approx 0.20(5)$ for the ripple regions. TEM, EDX and RBS measurements have also been carried out on the dot patterns. Here, the average compositions of Fe_xSi are about $Fe_{0.08}Si$ in the dots and $Fe_{0.03}Si$ in the flat region, respectively.

4. Scenario for pattern formation

Based on our experimental results, we propose a sequence of processes to describe the mechanism of pattern formation that relies on a completely different mechanism compared to the commonly applied continuum theories.

According to figure 7, the saturation coverage with Fe is already reached at a fluence of 1×10^{17} Xe cm^{-2}. According to TRIDYN calculations, saturation is already reached at 3×10^{16} Xe cm^{-2}. From figures 3(i), 5(a) and (d), it is shown that for a low coverage of

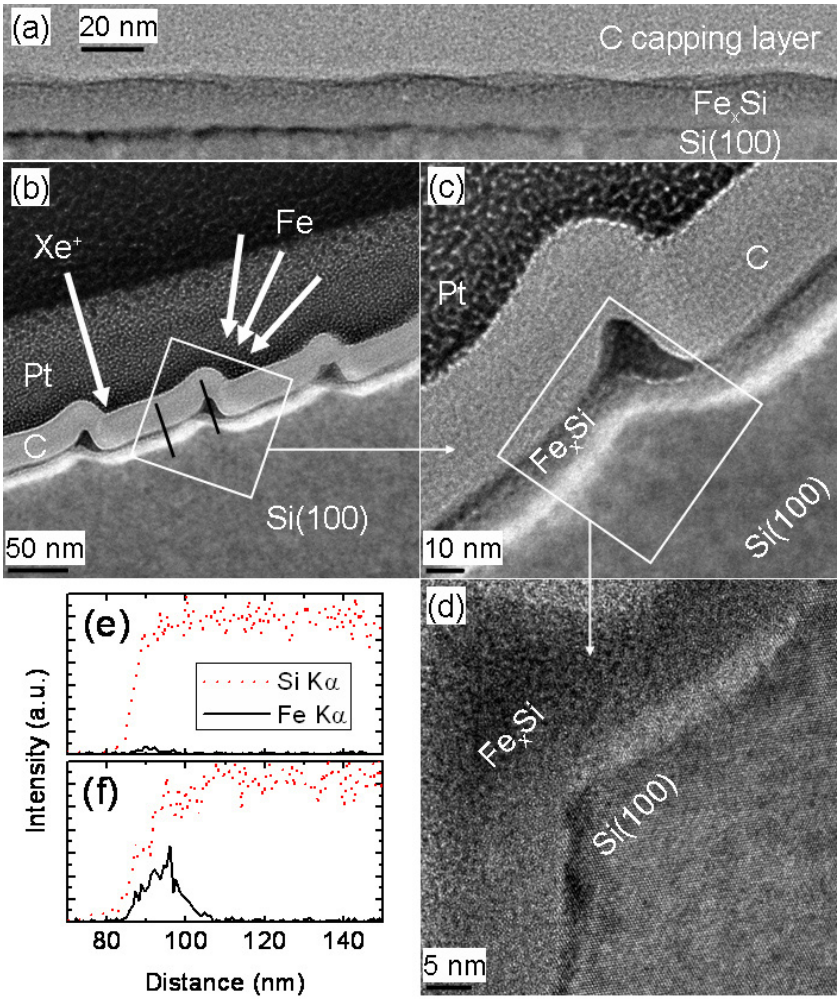

Figure 9. (a): Cross-sectional TEM image of a sample obtained after irradiation with 1.5×10^{17} Xe cm^{-2} and Fe coverage of 3.5×10^{15} at. cm^{-2} showing the onset of pattern formation. (b–d) Cross-sectional TEM images with increasing magnification of a sample surface region exhibiting ripple patterns corresponding to the sample shown in figure 3(d) (5×10^{17} Xe cm^{-2} and 5.4×10^{15} Fe cm^{-2}). (e) EDX-line scan through the ripple position. (f) EDX-line scan through the flat region between the ripples. The samples were coated with an amorphous carbon-capping layer prior to TEM sample preparation (see text).

1.8×10^{15} Fe cm^{-2} the Si surface is flat, even for a fluence of 5×10^{17} Xe cm^{-2}. For 3×10^{15} Fe cm^{-2}, the surface is still flat at 1×10^{17} Xe cm^{-2}. For 5×10^{15} Fe cm^{-2}, a weak irregular pattern appears at 1×10^{17} Xe cm^{-2}. Therefore, the saturation Fe coverage is reached before the patterns start to form. In addition, at fluences of 1×10^{17} Xe cm^{-2}, the surface region is already completely amorphized up to about 15 nm depth so that crystal structure effects can be ruled out. Therefore the initial steps of pattern formation are caused by none of the following: directional effects of the Fe-deposition, directional effects of the ion beam, and the Si crystal structure. Instead, we propose a phase separation of the amorphous Fe$_x$Si surface region into regions with higher and lower Fe content, driven by ion-induced diffusion. Preliminary cross-sectional

TEM analyses support an inhomogeneous composition in the flat amorphous surface layers with saturation Fe coverage. However, evidence of an initial phase separation is expected from scanning Auger microanalysis.

Ion-induced phase separation has been observed previously as a volume effect, e.g. in binary metal alloys [60]–[62], metal nanocrystal formation at Si/SiO_2 interfaces [63], FePt nanocrystal formation in Pt/Clayered films [64], ion-irradiated Cr/Cr coatings [65] and ion-irradiated sub-stoichiometric GeO_x films [66], and it was modeled using kinetic Monte Carlo simulations [60, 67, 68]. The Fe-Si system has a tendency to form FeSi and $FeSi_2$ alloys upon annealing to about 600–800 °C [69]–[71] or by ion beam mixing of Fe-Si bi-layers at lower temperatures, 450–550 °C [72]. The latter study demonstrates that ion irradiation promotes Fe_xSi alloy formation. For annealing of sub-nm Fe films on Si, the formation of two-dimensional (2D) $FeSi_2$ islands was observed [69]. Therefore, we may expect that in our experiments the 2D phase separation may be induced by low-energy Xe-ion irradiation. The ion irradiation itself would also have an opposite effect, because displacement events in the collision cascade may, to some extent, hinder the accumulation of Fe into Fe_xSi clusters or islands. As a balanced ion-beam-driven effect, a phase separation in Fe_xSi regions with variable Fe content may occur. Up to this stage, no pattern is formed, but only the Fe areal density becomes inhomogeneous.

For different local Fe concentrations of the amorphous Fe_xSi layer, we may expect slightly different local sputter yields for Si. We do not have to take into account the Fe sputter yield because we have reached dynamic equilibrium, so that the effective loss of Fe is zero. For higher Fe content, we expect a slightly lower Si sputter yield compared to regions with lower Fe content or pure Si. As a consequence, regions with higher Fe content are sputtered with a lower rate. Therefore, dot-like patterns will develop with increasing ion fluence. These initial dot patterns should be rather isotropic with no long-range order. This is confirmed by the FFT images of figures 3(f)–(h) and 5(a). In figure 5, it is observed that the pattern contrast increases with ion fluence, reaching eventually dot and ripple heights of about $h \approx 10\,\mathrm{nm}$ at a fluence of $\Phi = 5 \times 10^{17}\,\mathrm{Xe\,cm^{-2}}$. If such a pattern height results from the composition-dependent sputter yield, we can calculate the difference in sputter yield between Fe-rich dot and ripple regions Y_{dot} and Fe-poor intermediate regions Y_{int} from

$$\Delta Y = (Y_{\mathrm{int}} - Y_{\mathrm{dot}}) = h \times \frac{n}{\Delta\Phi}, \tag{1.1}$$

with fluence range $\Delta\Phi$ and atomic density n. For $\Delta\Phi = 5 \times 10^{17}\,\mathrm{Xe\,cm^{-2}}$ and $n \approx 5 \times 10^{17}\,\mathrm{cm^{-3}}$, we obtain a value of $\Delta Y \approx 0.1$, only about 6% of the Si sputter yield, which would be sufficient to generate the observed pattern height. From TRIDYN (or SRIM) simulations of the sputter yield of Fe_xSi for initial composition $x = 0.2$ and $x = 0.03$, we obtain $\Delta Y \approx 0.06 \pm 0.03$. Therefore, TRIDYN results support the idea that the composition-dependent sputter yield is sufficiently large to explain the observed pattern evolution.

When a pattern with a certain dot height is established, the directed deposition of atoms comes into play. Deposition occurs preferentially onto one side of the dots and also shadowing effects lead to a reduced deposition on the dot or ripple region opposite to the deposition direction. Therefore, we get preferential deposition in the dot and ripple regions and thus an additional local increase in the Fe concentration. When the Fe coverage is sufficiently large, dots may merge into short ripples and eventually a complete ripple pattern is generated. Due to the angular spread of the deposition directions, the ripples may develop a curvature, as can be seen in figures 3(d), 6(a) and (b). This curvature of the ripples may be responsible for the high defect density of the measured ripple patterns.

For oblique ion incidence, a ripple pattern already forms in the low fluence regime ($\sim 10^{16}$ ions cm^{-2}) driven by a Bradley–Harper-type mechanism. For example, for 5 keV Xe^+ irradiation of Si at 70°–75° ion incidence angle, a ripple pattern with 30 nm wavelength and wave vector parallel to the projected ion direction appears already at a fluence of 3×10^{15} Xe cm^{-2} [15]. For surfactant sputtering under such conditions, a ripple pattern exists before the steady-state coverage reaches its equilibrium value. The initial ripple pattern is then generated by the ion beam and the surfactants may modify this pattern, i.e. leading to relief-like structures or smooth surfaces, as observed for Ag, Pt or Au surfactants on Si [18].

The question arises as to whether keV heavy ions such as Xe are able to induce significant diffusion processes. For 5 keV Xe in Si, we find from SRIM about 150 displacements per ion. The overall shape of the collision cascade is roughly cylindrical around the ion path. About 60% of the ion's energy is released into phonon excitation, i.e. local vibrational excitations of Si atoms. Using the cylindrical thermal spike model [73], we can predict the number n_S of atoms within the collision cascade volume and also the number of rearrangements n_T due to phonon excitation within the cascade volume. For keV heavy ions in e.g. amorphous carbon [73], the ratio $n_\mathrm{T}/n_\mathrm{s}$ reaches a value of about $n_\mathrm{T}/n_\mathrm{S} \approx 3$ and n_S is of the order of 10^3 atoms (figure 16 and equation (57) in [73]). With these numbers, we can estimate the amount of ion-induced diffusion. Each incident Xe ion will rearrange about $n_\mathrm{T} \approx 3 \times 10^3$ atoms, which is much more than the 150 displaced atoms due to collisions. Therefore, the phonon excitation-induced thermal spike dominates over displacement collisions. Within a 15 nm thick amorphous Fe_xSi layer, we have about $\sigma = 7.5 \times 10^{16}$ atoms cm^{-2} with average atomic spacing $a \approx 0.3$ nm. An ion fluence of $\Phi = 1 \times 10^{17}$Xe cm^{-2} rearranges about $\Phi \cdot n_\mathrm{T} = 3 \times 10^{20}$ atoms cm^{-2} within this layer, or each atom of the layer undergoes about $N = \Phi \cdot n_\mathrm{T}/\sigma \approx 4000$ rearrangements. For a 3D random walk, the mean square distance is given by $\langle R_N^2 \rangle = 3Na^2$; with step distance $a \approx 0.3$ nm and $N \approx 4000$, we obtain $\sqrt{\langle R_N^2 \rangle} \approx 33$ nm. This estimate shows that ion-induced diffusion of Fe and Si atoms over distances sufficiently large to account for pronounced phase separation should be possible.

5. Discussion

In the absence of simultaneous deposition of surfactant atoms or in the absence of Fe as contamination of the Si surface, absolutely no nanopatterns are formed during normal ion incidence sputter erosion with 5 keV Xe ions and only flat surfaces are obtained. A pronounced self-organized pattern formation is triggered and driven by continuous Fe co-deposition from an adjacent steel sputter target irradiated with the same ion beam. Already for a fluence below 10^{17} Xe cm^{-2} a steady-state Fe coverage is established, which varied between 10^{15} and 10^{16} Fe cm^{-2} depending on the local Fe-deposition flux. The measured local Fe-deposition flux is in good agreement with a calculation of the flux of sputtered Fe atoms assuming a $\cos^y \theta$ angular distribution of sputtered atoms, a quadratic distance dependence and taking into account the local Fe atom incidence angle.

The AFM images in figures 3 and 5 emphasize the fact that the amount of Fe steady-state coverage is a key parameter for the formation of nanopatterns on the Si surface during normal incident ion beam sputtering. The Fe coverage determines the type of pattern, such as dot patterns, mixed dot and ripple patterns and ripple patterns. With increasing ion fluence, the pattern contrast increases, i.e. the dot and ripple height increases, but the type of pattern

remains unchanged. We find a critical Fe steady-state coverage for onset of dot formation (2×10^{15} Fe cm^{-2}), merging of dots to short ripples (4×10^{15} Fe cm^{-2}) and onset of ripple formation (6×10^{15} Fe cm^{-2}). The orientation of the ripples and chains of dots is perpendicular to the overall deposition direction of Fe atoms.

When dot patterns start forming at 2×10^{15} Fe cm^{-2} coverage, with increasing coverage the dot density decreases and the pattern contrast (dot height) increases. This continues until dots merge into short ripples. The rms roughness in this regime remains rather constant. At the onset of complete ripple pattern formation at 6×10^{15} Fe cm^{-2}, the roughness increases further and reaches a larger saturation value.

The ripple patterns are highly distorted, showing a large number of dislocations and also a slight curvature of ripples. This is probably caused by the distribution of Fe surfactant deposition directions with an azimuthal angle of about $\pm 45^\circ$ around the average deposition direction and grazing incidence angles between 75° and 90° with respect to the surface normal.

Compared to the sputter yield $Y_{\mathrm{Si}} \approx 1.7$ of pure Si, the overall sputter yield of patterned Si with Fe steady-state coverage is larger and may reach values of up to $Y \approx 3.4$. The main reason for this increase is the roughness of the patterns itself, leading to locally varying ion incidence angles and corresponding sputter yield. A sputter yield amplification effect plays a minor role.

AFM height profiles and also TEM images reveal a highly asymmetric shape of the ripples that is related to the Fe surfactant deposition direction. TEM and EDX analyses show that an amorphous $\mathrm{Fe}_x\mathrm{Si}$ phase with a thickness of 15–25 nm is formed, which can be explained by ion beam damage. The Fe concentration is inhomogeneous and reaches values of $x \approx 0.20(5)$ in the ripple and dot regions and $x \approx 0.03(1)$ in the flat intermediate regions.

The inhomogeneous Fe distribution is, in our opinion, initially caused by ion-induced diffusion and phase separation processes and eventually enhanced due to the directed deposition of Fe. Moreover, the slight inclination of the flat regions in between ripples and dots with inclination angles of up to 8° with respect to the global surface normal may be due to sputtering of the steep slopes of the patterns and re-deposition into the intermediate regions. Ion-induced diffusion is also seen as a major contribution for the decrease in the dot area density and the merging of dots to ripples at nearly constant rms roughness. The increase in pattern contrast with increasing ion fluence can be explained by a composition-dependent sputtering yield.

Preliminary cross-sectional TEM analyses support an inhomogeneous composition in the initial flat amorphous surface layers with saturation Fe coverage. However, clear evidence of an initial phase separation may be provided e.g. with scanning Auger microanalysis, which should show a lateral non-uniform Fe concentration. Analyses of some samples are currently under way. To support the assumption that directed deposition of surfactant atoms has no influence on the initial pattern formation, one could perform analogous experiments using surfactant atoms, which do not tend to phase separate when forming an amorphous compound layer with Si. In particular, we expect that the same experiment with a silicon target as the source of surfactants should yield a flat and pattern-free surface after erosion. On the other hand, systems with a strong tendency to phase separate or with strong surface diffusion of surfactants should produce rather distinct patterns. Candidates for that are Ag and Mo surfactants. Experiments outlined here are currently under way.

An open question is whether the patterns are static or dynamic. For sputtering of pure Si at oblique ion incidence, it was observed that the ripple patterns move with a certain

velocity [74] in agreement with theoretical predictions [3]. In the case of normal ion incidence, we would not expect such a dynamic behavior. However, it may be induced by the directed asymmetric Fe deposition, leading to the local asymmetric patterns and thus asymmetric local sputter rates.

A further challenge is to reduce the pattern defect density and to create more uniform dot and ripple patterns, which may then be of interest for e.g. optical or sensor applications requiring large-area nanopatterned surfaces. This may be achieved by a more precisely directed surfactant deposition using a more distant sputter target.

6. Conclusion

We have shown that directed deposition of Fe surfactant atoms triggers and drives the self-organized formation of nanopatterns during ion beam sputter erosion of Si substrates at normal ion incidence. Without these surfactants or contaminations, no patterns were formed and the surfaces remained flat. The Fe surfactant coverage rapidly reached a steady-state value. We have observed the critical values of this coverage for the onset of dot formation, merging of dots and onset of ripple formation between 2×10^{15} and 6×10^{16} Fe cm^{-2}. Thus, the Fe coverage determines the pattern type, whereas the ion fluence determines the pattern contrast. The pattern orientation is determined by the Fe-deposition direction. Continuous Fe surfactant deposition in combination with ion irradiation gives rise to ballistic mixing, damage formation and most probably strong ion-induced diffusion. In particular, ion-induced diffusion, ion-induced phase separation and a composition-dependent sputter yield are seen as major processes leading to dot and ripple pattern formation. Therefore, our results support a novel mechanism for pattern formation by ion beam erosion, which is different from the commonly applied mechanisms based on curvature-dependent sputter yields and surface diffusion. Recently, at the IBMM 2010 conference, Zhou and Lu [75] presented a continuum model to describe the surface evolution of Si during normal incidence ion sputtering with Fe incorporation. Their model includes surface-stress-induced instability and preferential sputtering as additional mechanisms for pattern formation. At the same conference Castro and Cuerno [76] introduced ion irradiation-induced viscous flow as a novel contribution to surface pattern formation. This underlines that ion-induced effects on the volume of the amorphized layer generated by the ion beam on top of the substrate may have relevant contributions to pattern formation.

Surfactant sputtering turns out to be a versatile method for creating novel surface nanopatterns with manifold possible applications. Our results provide the relevant parameters to achieve well-controlled pattern formation. They open the door to quantitatively reveal the mechanisms of pattern formation and provide valuable input to develop new theoretical models based on ion-induced diffusion and phase separation for surfactant-driven pattern formation.

Acknowledgments

We acknowledge fruitful discussions with Professor R Jayavel of Anna University, Chennai, India. This work was financially supported by the Deutsche Forschungsgemeinschaft (DFG) under grant no. HO1125/20-1.

References

[1] Valbusa U, Borangno C and de Mongeot F R 2002 *J. Phys.: Condens. Matter.* **14** 8153
[2] Carter G 2001 *J. Phys. D: Appl. Phys.* **34** R1
[3] Aste T and Valbusa U 2005 *New J. Phys.* **7** 122
[4] Hartmann A K, Kree R and Yasseri T 2009 *J. Phys.: Condens. Matter.* **21** 224015
[5] Vogel S and Linz S J 2006 *Europhys. Lett.* **76** 884
[6] Chen Y J, Wang J P, Soo E W, Wu L and Chong T C 2002 *J. Appl. Phys.* **91** 7323
[7] Chan W L and Chason E 2007 *J. Appl. Phys.* **101** 121301
[8] Bisio F, Moroni R, Buatier de Mongeot F, Canepa M and Mattera L 2006 *Appl. Phys. Lett.* **89** 052507
[9] Zhang K, Uhrmacher M, Hofsäss H and Krauser J 2008 *J. Appl. Phys.* **103** 083507
[10] Fu Y, Bryan N and Zhou W 2004 *Opt. Express* **12** 227
[11] Bradley R M and Harper J M 1988 *J. Vac. Sci. Technol.* A **6** 2390
[12] Park S, Kahng B, Jeong H and Barabási A L 1999 *Phys. Rev. Lett.* **83** 3486
[13] Munos-García J, Gago R, Vazquez L, Angel, Sánchez-García J and Cuerno R 2010 *Phys. Rev. Lett.* **104** 026101
[14] Davidovitch B, Aziz M and Brenner M P 2007 *Phys. Rev.* B **76** 205420
[15] Zhang K, Rotter F, Uhrmacher M, Ronning C, Hofsäss H and Krauser J 2007 *Surf. Coat. Technol.* **201** 8299
[16] Carter G and Vishnyakov V 1996 *Phys. Rev.* B **54** 17647
[17] Habenicht S, Bolse W, Lieb K P, Reimann K and Geyer U 1999 *Phys. Rev.* B **60** R2200
[18] Hofsäss H and Zhang K 2008 *Appl. Phys.* A **92** 517
[19] Hofsäss H and Zhang K 2009 *Nucl. Instrum. Methods* B **267** 2731
[20] Zhang K, Hofsäss H and Zutz H 2010 *Nucl. Instrum. Methods* B **268** 1967
[21] Hofsäss H, Zhang K and Zutz H 2009 *Nucl. Instrum. Methods* B **267** 1398
[22] Punzel J and Hauffe W 1972 *Phys. Status Solidi a* **14** K97
[23] Wehner G K and Hajicek D J 1971 *J. Appl. Phys.* **42** 1145
[24] Wehner G K 1985 *J. Vac. Sci. Technol.* A **3** 1821
[25] Rossnagel S M, Robinson R S and Kaufman H R 1982 *Surf. Sci.* **123** 89
[26] Sen A K and Ghose D 1991 *J. Mater. Sci. Lett.* **10** 1304
[27] Panitz J K G 1991 *J. Micromech. Microeng.* **1** 52
[28] Berg S and Katardjiev I V 1999 *J. Vac. Sci. Technol.* A **17** 1916
[29] Biersack J P, Berg S and Nender C 1991 *Nucl. Instrum. Methods* B **59/60** 21
[30] Nender C, Katardjiev I V, Biersack J P, Berg S and Barklund A M 1994 *Radiat. Eff. Defects Solids* **130** 281
[31] Berg S and Katardjiev I 1996 *Surf. Coat. Technol.* **84** 353
[32] Berg S, Barklund A, Gelin B, Nender C and Katardjiev I 1992 *J. Vac. Sci. Technol.* A **10** 1592
[33] Morishita M and Okuyama F 1990 *J. Vac. Sci. Technol.* A **8** 3295
[34] Tanemura M, Yamauchi H, Yamane Y, Okita T and Tanemura S 2004 *Nucl. Instrum. Methods* B **215** 137
[35] Ozaydin-Ince G, Özcan A S, Wang Y, Ludwig K F, Zhou H, Headrick R L and Siddons D P 2005 *Appl. Phys. Lett.* **87** 163104
[36] Ozaydin-Ince G and Ludwig K F Jr 2009 *J. Phys.: Condens. Matter.* **21** 224008
[37] Ma X L, Shang N G, Lee C S and Lee S T 2002 *J. Mater. Sci. Technol.* **18** 173
[38] Shang G, Meng F Y, Au' F C K, Li Q, Lee C S, Bello I and Lee S T 2002 *Adv. Mater.* **14** 1308
[39] Tanemura M, Okita T, Tanaka J, Yamauchi H, Miao L, Tanemura S and Morishima R 2005 *Eur. Phys. J.* D **34** 283
[40] Facsko S, Desorsky T, Koerdt C, Trappe C, Kurz H, Vogt A and Hartnagel H L 1999 *Science* **285** 1551
[41] Facsko S, Bobek T, Kurz H, Dekorsky T, Kyrsta S and Cremer R 2002 *Appl. Phys. Lett.* **80** 130
[42] Facsko S, Bobek T, Dekorsky T and Kurz H 2001 *Phys. Status Solidi* b **224** 537
[43] Paramanik D and Varma S 2008 *Nucl. Instrum. Methods* B **266** 1257
[44] MacLaren S W, Baker J E, Finnegan N L and Loxton C M 1992 *J. Vac. Sci. Technol.* A **10** 468

[45] Le Roy, Barthel E, Brun N, LeLarge A and Søendergârd E 2009 *J. Appl. Phys.* **106** 094308
[46] Kahng B, Jeong H and Barabási A L 2001 *Appl. Phys. Lett.* **78** 805
[47] Ziberi B, Cornejo M, Frost F and Rauschenbach B 2009 *J. Phys.: Condens. Matter.* **21** 224003
[48] Frost F, Ziberi B, Schingler A and Rauschenbach B 2008 *Appl. Phys.* A **91** 551
[49] Ziberi B, Frost F, Höche Th and Rauschenbach B 2005 *Phys. Rev.* B **72** 235310
[50] Ziberi B, Frost F and Rauschenbach B 2005 *Appl. Phys. Lett.* **87** 033113
[51] Ziberi B, Frost F and Rauschenbach B 2006 *J. Vac. Sci. Technol.* A **24** 1344
[52] Ling L, Li W, Qi L, Lu M, Yang X and Gu C 2005 *Phys. Rev.* B **71** 155329
[53] Macko S, Frost F, Ziberi B, Förster D F and Michely T 2010 *Nanotechnology* **21** 085301
[54] Sánchez-García J A, Gago R, Caillard R, Redondo-Cubero A, Martin-Gago J A, Palomares F J, Fernández M and Vázques L 2009 *J. Phys.: Condens. Matter.* **21** 224009
[55] Hofsäss, Binder H, Klumpp T and Recknagel E 1994 *Diam. Relat. Mater.* **3** 137
[56] Ziegler J, Biersack J P and Ziegler M D 2008 *SRIM—The Stopping and Ranges of Ions in Solids* (Chester: SRIM Co.) http://srim.org
[57] Möller W, Eckstein W and Biersack J P 1988 *Comput. Phys. Commun.* **51** 355
[58] Gnaser H 2007 *Sputtering by Particle Bombardment—Experiments and Computer Calculations from Threshold to MeV Energies (Topics in Applied Physics* vol 110*)* ed R Behrisch and W Eckstein (Berlin: Springer) pp 231–329
[59] Biersack J P and Eckstein W 1984 *Appl. Phys.* A **34** 73
[60] Chee S W, Stumphy B, Vo N Q, Averback R S and Bellon P 2010 *Acta Mater.* **58** 4088
[61] Tai K P, Dai X D and Liu B X 2006 *Appl. Phys. Lett.* **88** 184103
[62] Krasnochtchekov P, Averback R S and Bellon P 2005 *Phys. Rev.* B **72** 174102
[63] Heinig K H, Müller T, Schmidt B, Strobel M and Möller W 2003 *Appl. Phys.* A **77** 17
[64] Bera S *et al* 2006 *J. Appl. Phys.* **99** 074301
[65] Hovsepian P E *et al* 2005 *Surf. Coat Technol.* **200** 1572
[66] Batra Y, Kabiraj D, Kumar S and Kanjilal D 2007 *J. Phys. D: Appl. Phys.* **40** 4568
[67] Enrique R A and Bellon P 2001 *Phys. Rev.* B **63** 134111
[68] Krasnochtchekov P, Averback R S and Bellon P 2007 *Phys. Rev.* B **75** 144107
[69] Balashev V V, Korobtsov V V, Pisarenko T A, Chusovitin E A and Galkin K N 2010 *Phys. Solid State* **52** 397
[70] Lal C, Dhunna R and Jain I P 2008 *Mater. Sci. Semicond. Proc.* **11** 1
[71] Ayache R, Bouabellou A, Eichhorn F and Richter E 2004 *Rev. Adv. Mater. Sci.* **8** 97
[72] Milosavljevic M, Dhar S, Schaaf P, Bibic N, Han M and Lieb K P 2000 *Appl. Phys. A.* **71** 43
[73] Hofsäss H, Feldermann H, Merk R, Sebastian M and Ronning C 1998 *Appl. Phys.* A **66** 153
[74] Habenicht S, Lieb K P, Koch J and Wieck A D 2002 *Phys. Rev.* B **65** 115327
[75] Zhou J and Lu M 2011 The mechanism of Fe impurity motivated ion-nanopatterning of Si(100) surfaces *IBMM 2010 Conf. (Montreal, Canada, 22–27 August 2010) Nucl. Instr. Meth.* B at press
[76] Castro M and Cuerno R 2011 Surface nanopatterning via ion bombardment: viscous flow vs sputtering *IBMM 2010 Conf. (Montreal, Canada, 22–27 August 2010) Nucl. Instr. Meth.* B at press